Inhalation Toxicology, 2012; 24(8): 492–505

ISSN 0895-8378 print/ISSN 1091-7691 online
DOI: 10.3109/08958378.2012.694494

informa
healthcare

RESEARCH ARTICLE

Local deposition fractions of ultrafine particles in a human nasal-sinus cavity CFD model

Qin Jiang Ge[1], Kiao Inthavong[1], and Ji Yuan Tu[1,2]

[1]*School of Aerospace, Mechanical and Manufacturing Engineering, RMIT University, Australia and* [2]*Department of Building Science, Tsinghua University, Beijing, China*

Abstract

Ultrafine particle deposition studies in the human nasal cavity regions often omit the paranasal sinus regions. Because of the highly diffusive nature of nanoparticles, it is conjectured that deposition by diffusion may occur in the paranasal sinuses, which may affect the residual deposition fraction that leaves the nasal cavity. Two identical CFD models of a human nasal cavity, one with sinuses and one without, were reconstructed from CT-scans to determine the uptake of ultrafine particles. In general, there was little flow passing through the paranasal sinuses. However, flow patterns revealed that some streamlines reached the upper nasal cavity near the olfactory regions. These flow paths promote particle deposition in the sphenoid and ethmoid sinuses. It was found that there were some differences in the deposition fractions and patterns for 5 and 10 nm particles between the nasal-sinus and the nasal cavity models. This difference is amplified when the flow rate is decreased and at a flow rate of 4 L/min the maximum difference was 17%. It is suggested that evaluations of nanoparticle deposition should consider some deposition occurring in the paranasal sinuses especially if flow rates are of concern.

Keywords: Nasal cavity, sinus, nanoparticle, CFD

Introduction

Particle deposition studies caused by inhalation through the nasal cavity have been performed using (i) computational fluid dynamics (CFD) methods (Schroeter et al., 2006a), (ii) replicate cast models of a nasal cavity (Cheng et al., 2001; Kelly et al., 2004) or by using and (iii) *in-vivo* human subjects (Cheng et al., 1995; Cheng et al., 1996b). The particle deposition data obtained from these methods are used interchangeably to compare and verify results. In CFD and replicate cast methods the nasal cavity is extracted from MRI or CT-scans of the respiratory system, and often the end product omits the paranasal sinuses. However, deposition data on a human subject is inclusive of the paranasal sinuses and it is unknown to what extent this influences the total and local deposition fractions in the nasal cavity.

According to Cheng et al. (1996a) aerosol deposition in the human respiratory airways is strongly influenced by three major factors: physical (particle diameter, shape, and density), physiological (respiratory ventilation and pattern), and morphological (airway size and shape). Deposition of micron sized particles in the nasal cavity and the lung conductive airways is largely due to the particle inertia, and in general, significant for particles with aerodynamic diameters approximately greater than ~2 μm.

Studies have shown that the sharp curvatures in the nasal cavity airway that change the airflow direction are responsible for inertial deposition of micron particles (Inthavong et al., 2006, 2011a). This is particularly significant at the entrance to the main nasal passage and at the nasopharynx where the flow exhibits 90° curvatures. Inertial deposition mechanisms rely on flow convection which transports the particles before a sharp curvature is present. With regards to micron particle deposition in the maxillary sinus, (Xiong et al., 2008) indicated that little flow exchange occurred between the inner and outer

Address for Correspondence: Prof Jiyuan Tu, School of Aerospace, Mechanical and Manufacturing Engineering, RMIT University, PO Box 71, Bundoora Vic 3083, Australia. Tel: +61-3-9925 6191. Fax: +61-3-9925 6108. E-mail: jiyuan.tu@rmit.edu.au

(Received 28 February 2012; revised 09 May 2012; accepted 14 May 2012)

aspects of the paranasal sinuses. This suggests that it is unlikely that micron particles will be lost to the sinus regions and CFD and replicate cast studies omitting the sinus regions is applicable.

On the other hand, ultrafine particles are dominated by diffusion and their deposition onto its surrounding surfaces is reliant on a low convection to diffusion ratio (i.e. Peclet number). It should be noted that ultrafine particles are defined as particles between 1–100 nm in size which coincidently is the same size range definition that is often used for nanoparticles (Auffan et al., 2009), and hence these two terms are often used interchangeably in the literature (Longest & Xi, 2007b). In this study the term ultrafine particles will be used to encompass particles 1–100 nm. If the flow rate through the nasal cavity is sufficiently low, the diffusion transport of ultrafine particles may be significant enough for the particles to pass into the paranasal sinuses. This suggests that ultrafine particles may be lost to the sinus regions (to what extent is unknown) and that the residual deposition fraction that leaves the nasal cavity and enters the downstream airway regions such as the trachea and bronchial region may need to be reconsidered.

The paranasal sinuses (maxillary, sphenoid, ethmoid and frontal) are air-filled spaces connected to the nasal cavity by narrow passageways called ostia. The exact biologic function of the sinuses is uncertain but are thought to contribute to the following: reduction of the weight of the front of the skull; act as a resonating chamber for voice production; humidifying, heating, and filtering of inhaled air through mucus secretions; and absorption of any force impacting on the face or skull (Keir, 2009).

Deposition of ultrafine particles within these sinuses or around the ostia is important due to their potential clinical ramifications. Ultrafine particles that cause irritation or an allergic reaction can result in swelling of the ostium, impaired sinus mucus drainage and subsequent sinusitis, a condition that exacerbates existing respiratory ailments (Slavin, 1988). Furthermore, the paranasal sinuses (in particular the maxillary sinus) are a potential site for malignancy. For example, it is well established that there are links between tobacco smoke, formaldehyde (Halperin et al., 1983), and nasal cancer, but studies have shown that inhalation of airborne toxic ultrafine particles such as wood dust (Elwood, 1981), air pollution and fumes (Calderón-Garciduenas et al., 2000) may be a significant risk factor in the development of paranasal sinus cancer. As nanotechnology plays a bigger part in society and day to day exposure to ultrafine particles increases, diffusion of these potentially carcinogenic ultrafine particles into the sinuses could be a significant contributor to malignant tumors of the sinuses. Paranasal sinus tumors are often diagnosed late and thus have a very poor prognosis. To date, nearly all CFD studies of particle deposition through the nasal cavity have neglected the paranasal sinuses, although there have been two studies of air flow distribution through the nasal cavity that include the paranasal sinuses (Lindemann et al., 2005; Xiong et al., 2008).

Therefore, the aim of this study is to investigate the flow patterns in the nasal cavity, in the paranasal ostium and its corresponding sinus, and to determine the uptake of ultrafine particles with a focus on the ostium region that may occlude due to deposition. The uptake of the ultrafine particles within the nasal-sinus model and in a nasal cavity model for different particle sizes is given. In addition, special attention is made to the modeling of the Brownian diffusion process to ensure that the predictions of the ultrafine particles are reliable. Micron sized particles which can be defined as anything greater than 1 μm (although PM2.5 or fine particles – aerodynamic diameters <2.5 μm and PM10 or coarse particles – aerodynamic diameters between 2.5 μm and 10 μm, are the standard classifications in toxicology), are not reported here as our preliminary testing found that micron particles from 1–100 μm showed negligible differences between the nasal-sinus model, and nasal cavity model.

Method

Computational models

Four geometries were created for this study – a straight pipe, a 90° bend pipe, a human nasal cavity with paranasal sinuses included, and the same nasal cavity model without sinuses (Figure 1). Table 1 the geometries detailing significant dimensions and the computational boundary conditions that are applied. The pipe models are used to validate the Brownian model and to ensure it is reliable before applying it to the more complex nasal cavity. For the nasal cavity model, CT-scans of a healthy nose from a 51-year-old Asian male, was obtained. The scans were performed using a whole body scanner by Phillips® at No.3 Hospital, Shanghai with the subject's approval and consent for participation in this study. The scan protocol included slice thickness is 0.625 mm, and the single pixel space is 0.976 × 0.976 mm, a 300 × 500 mm field of view, 30 kV peak, and 200 mA.

The outline of the model was segmented from the CT-scans and a computational mesh for CFD analysis was applied. Two nasal cavity models were reconstructed from the same CT-scans, and are labeled as NC02 (nasal cavity without paranasal sinuses) and NC02-S (nasal cavity with paranasal sinuses), noting that the difference in the labels is the character S to denote the addition of the sinuses. The geometry of the NC02-S model is shown in Figure 1c. The length from the anterior most region to the posterior nasopharynx region is approximately 9 cm, while the height from the main nasal passage floor to the superior tip of the frontal sinus is approximately 7 cm. It should be noted that the surface walls of the computational model are smooth and rigid, and lacks nose hair and mucous. For ultrafine particles, where the deposition is diffusion dominant, the presence of nose hair can have some impact on the deposition. This phenomenon is yet to be researched.

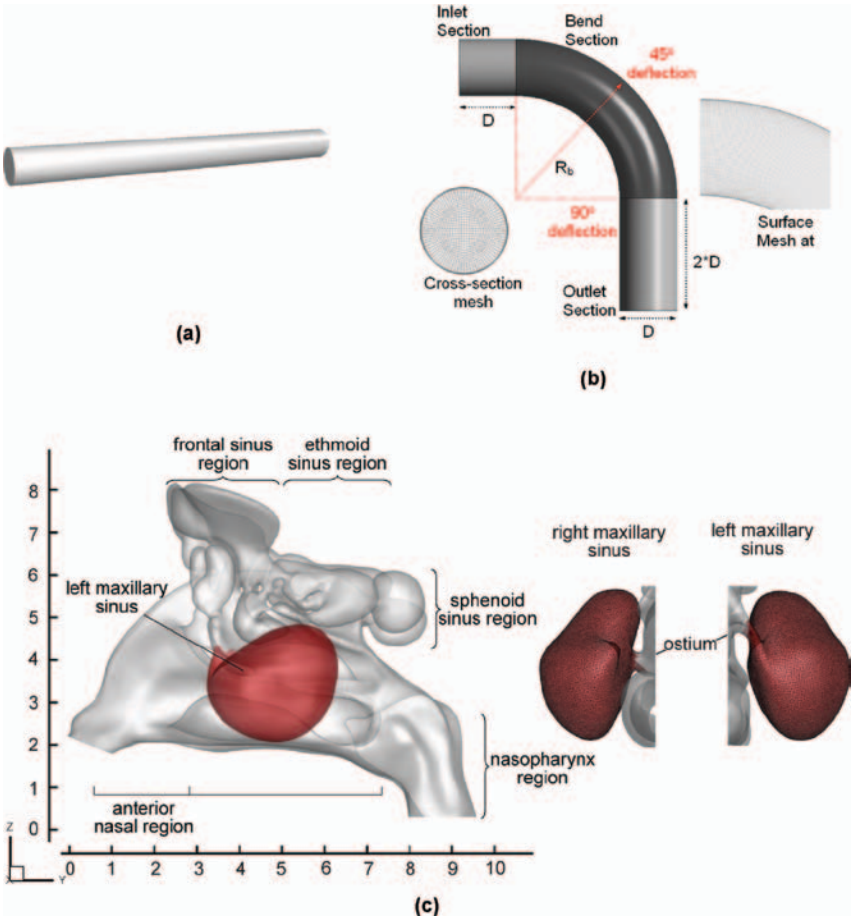

Figure 1. CFD geometries used in this study for (a) straight pipe, (b) 90° bend pipe, and (c) nasal cavity with sinus model.

Table 1. Dimensions and details of the geometries considered in this study.

	Inlet hydraulic diameter (D_h)	Radius of curvature, R_b	Inlet flow rate (L/min)	Inlet Renumber	Mesh size
Straight pipe	0.45 cm	–	1	322	750,000
			10	4840	
90° bend pipe	0.46 cm	1.43 cm	1.052	305	550,000
Nasal cavity without sinus (NC02)	1.0 cm	–	4	255	3.0 million
			10	642	
Nasal cavity with sinus (NC02-S)	1.0 cm	–	4	278	4.0 million
			10	705	

The meshing scheme used a hybrid mesh that included six-prismatic layers with an inner tetrahedral core. Grid independence based on velocity profiles at the outlet was performed (up to 10 million cells) where the optimum number of cells (3 million for NC02 and 4 million for NC02-S) for each geometry is given in Table 1, along with dimensions and details of the flow rate. This implies that the geometries showed less than 1% change in velocity profiles when the mesh was further refined.

The influence of computational smoothing on airflow resistance and particle deposition has been discussed in Schroeter et al. (2011). The models used in this study underwent 5% level of smoothing to ensure that any artificial residual artefacts persisting from the scanned images were omitted from the final computational model. Given that images obtained from CT-scans are more prone to artefacts than other conventional radiographs, the level of smoothing applied allowed a compromise between retention of real geometry artefacts (e.g. overlying mucus) to artificially created artefacts caused by CT-scans and its segmentation (e.g. streaking, distortion and shading due inconsistency and inaccuracy of scanner, or patient movement or the presence of metallic materials in or on the patient) and CAD file interpretations.

Fluid modeling

The geometries were inputted into a commercial CFD code, Ansys-FLUENT v12.1, where the governing equations for fluid flow under steady-state conditions were modeled. Flow rates of 1, and 10 L/min were used for the straight pipe and 90° bend pipe while low steady flow rates of 4, and 10 L/min were used for the nasal cavity to allow similar comparisons with *in-vivo* data at 10 L/min (Cheng et al., 1996a), *in-vitro* replicate cast deposition data at 4, 10 L/min (Cheng et al., 1995; Kelly et al., 2004), and numerical studies (Zamankhan et al., 2006; Shi et al., 2008). The inspiratory flow rates for adults can range between 5–12 L/min for light breathing and 12–40 L/min for non-normal conditions such as during exertion and physical exercise. Usually breathing switches from pure nasal flow to oral–nasal flow at this higher range. Interestingly Robert (2001) tested 68 patients to obtain forced inspiratory nasal flow–volume curves, which showed that some inspiratory peak flows reached up to 150 L/min, although this is highly unsustainable over any breathing cycle.

Up to a flow rate of 15 L/min the flow regime in the respiratory airways has been determined as dominantly laminar (Hahn et al., 1993; Swift & Proctor, 1977b; Kelly et al., 2000; Zamankhan et al., 2006), although traces of turbulent flow structures may exist. There is some debate to the correct treatment of the flow field as laminar or transitional turbulence. Like many unstable flows within complex geometries, the critical flow rate and hence the critical Reynolds number (Re_{cr}) at which the flow transitions from a laminar regime cannot be succinctly defined, nor can it be applied generally to all nasal cavities which inherently possess geometry differences. The varying critical Re is mainly due to sharp and sudden changes in the nasal cavity geometries that create diverging flows and flow separation, all contributing to flow instability. Experimental studies by Swift and Proctor (1977a) and Kelly et al. (2000) have suggested that a laminar flow regime dominates for low flow rates around 10 L/min. Hahn et al. (1993) results also concur where a flow rate for a single nasal chamber subjected to a flow rate of 10.8 L/min (~21.6 L/min for both nasal chamber sides) resulted in flow patterns that appeared laminar-like suggesting that for normal resting breathing, laminar-like flow dominates much of the nasal cavity. At higher flow rates of 33.6 and 66 L/min (~67.2 and 132 L/min for both nasal chamber sides), the flow was described as turbulent. Further experimental results by Churchill et al. (2004) showed that for ten nasal replicate cast models, the average rate at which flow switched from transitional to turbulent was 11 L/min. Despite this, a survey of more recent numerical simulations of realistic nasal airways show a consensus among researchers in using a laminar flow for flow rates less than 20 L/min (Schroeter et al., 2006b; Garcia et al., 2007). In this study a laminar flow model is used to focus on the diffusion process of the ultrafine particles and because of the low flow rates (≤10 L/min).

The steady-state continuity and momentum equations for the gas phase (air) in Cartesian tensor notation can be cast as:

$$\frac{\partial}{\partial x_i}\left(\rho_g u_i^g\right)=0 \tag{1}$$

$$u_j^g\frac{\partial u_i^g}{\partial x_j}=-\frac{1}{\rho}\frac{\partial p_g}{\partial x_i}+\frac{\partial}{\partial x_j}\left(\nu_g\frac{\partial u_i^g}{\partial x_j}\right) \tag{2}$$

where u_i^g is the i-th component of the time averaged velocity vector and ρ_g is the air density. The equations were discretized with the QUICK scheme while the pressure-velocity coupling was resolved through the SIMPLE method.

Particle flow modeling

For a low volume fraction of dispersed phase (particles), the Lagrangian approach with one-way coupling is used, i.e. the airflow transports the particles, but the effect of particle movements on the flow is neglected. In this approach, the airflow field is first simulated, and then the trajectories of individual particles are tracked by integrating a force balance equation on the particle, which can be written as:

$$\frac{du_i^p}{dt}=F_D+F_g+F_E \tag{3}$$

F_D is the drag force per unit particle mass taking the form of Stokes' drag law (Ounis et al., 1991) defined as,

$$F_D=\frac{\left(u_i^g-u_i^p\right)}{\tau_p} \tag{4}$$

where τ_p is the particle response time defined as

$$\tau_p=\frac{18\mu}{d_p^2\rho_p C_c}.$$

F_g is the gravity term, which is defined as

$$F_g=\frac{g(\rho_p-\rho_g)}{\rho_p} \tag{5}$$

and ρ_p and ρ_g denotes the density of particle material and air, respectively. C_c is the Cunningham correction factor to Stokes' drag law, which can be calculated from,

$$C_c=1+\frac{2\lambda}{d_p}\left(1.257+0.4e^{-\left(1.1d_p/2\lambda\right)}\right) \tag{6}$$

where λ is the mean free path of air, assumed to be 65 nm. Amplitudes of the Brownian force components are of the form,

$$F_B = \zeta\sqrt{\frac{\pi S_0}{\Delta t}} \tag{7}$$

where ζ is a zero mean, unit variance independent Gaussian random numbers. Δt is the time-step for particle integration, and S_o is a spectral intensity function,

$$S_0 = \frac{216\nu k_B T}{\pi^2 \rho d_p^5 \left(\frac{\rho_p}{\rho}\right)^2 C_c} \tag{8}$$

where T is the absolute temperature of air (an isothermal flow of 298 K is assumed), and k_B is the Boltzmann constant. It is noted that the Saffman lift force, for the range of ultrafine particles used in this study, is negligible and is not included in Equation (3). Particle rebounding from the surfaces is ignored and particle deposition is determined when the distance between the particle centre and a surface is less than or equal to the particle radius. The particle tracking is then terminated.

The Eulerian species/components approach to modeling the nanoparticle diffusion involves a single mixture fluid with the nanoparticles treated as a chemical species. A scalar *c*, representing the concentration of the nanoparticles is applied to the transport equation as:

$$\frac{\partial(u_j c)}{\partial x_j} = \frac{\partial}{\partial x_j}\left[\left(\widetilde{D} + \frac{\nu T}{S}\right)\frac{\partial c}{\partial x_j}\right] \tag{9}$$

which neglects the effects of particle inertia. Longest and Xi (2007a) showed that the effects of particle inertia plays a minor role in ultrafine aerosol deposition and that inertia effects could be neglected for particle Stokes numbers below 5×10^{-5}.

Boundary conditions and numerical solution

In order to achieve a fully developed flow for the straight and 90° bend pipes, an additional separate pipe 5D in length with the same cross-section and mesh were simulated with periodic boundaries applied. When the flow reached a fully developed state the velocity profile from the periodic straight pipe model was extracted and used as the inflow condition at the inlet of the 90° bend pipe and the straight pipe. Two flow rates were considered for the straight pipe, 1 L/min, and 10 L/min. For the nasal cavity, inhalation is induced through a pressure difference between the nostril inlets (P_{in} = 0Pa) and the nasopharynx outlet (P_{out}) that is set to a negative pressure relative to atmospheric pressure that is caused by the movement of the diaphragm. This is a more realistic representation of the inhalation cycle that considers the effects of nasal patency that is captured by the CT-scans of the airway.

Past experimental and numerical studies of airflow patterns in the nasal cavity have defined at the flow field at the nostril inlet by enforcing a fixed velocity or mass flow rate boundary condition (Xiong, Zaman). Where both cavities of the nose were used an equivalent flow rate at each nostril gives the presumption of an equivalent flow distribution through each cavity, before the flow merges at the naospharynx, which may not occur given that the flow is induced by a pressure difference from the extension and contraction of the diaphragm. In addition the use of a single cavity with a nasopharynx extension does not capture the airflow mixing patterns caused by the merging of the two cavities in the nose. During normal nasal physiology, one the nasal cavity is normally asymmetrical where one nasal passage is usually more patent than the other. This asymmetry is referred to as the nasal cycle which is a result of congestion (swelling) of the erectile tissue (cavernous tissues of the mucosa) in one nasal cavity while at the same time decongestion (shrinking) occurs to the erectile tissue in the other cavity. The airflow through each nasal cavity is then governed by the resistance caused by the cross-sectional area of each airway which can be captured by using the pressure difference boundary condition approach.

Particles in the pipe simulation were released from an evenly dispersed circular region 0.01 m from the inlet to prevent any spurious data occurring due to random particles exiting the inlet upon immediate release. Furthermore, a particle was located at no less than 0.1 mm away from the wall to eliminate artificial immediate deposition on the walls due to the stochastic nature of the Brownian motion model. In the Lagrangian tracking scheme, u_i^g found in the slip velocity (u_i^g–u_i^p) in Equation 4 is defined from the cell centre and a particle within any part of that cell takes u_i^g from the cell centre. For cells adjacent to the wall boundaries, the velocity profile should approach zero at the wall rather than be uniform throughout the cell. Therefore, a near wall interpolation (NWI) is applied to account for the diminishing velocity that approaches zero at the wall. Details of the scheme are given in Inthavong et al. (2011b).

The small diameter size of ultrafine particles results in very small particle response times which produce the so-called stiff ordinary differential equation problem. This makes the Runge-Kutta algorithm prohibitive in solving the particle trajectory equation (Equation 3). Instead the implicit Euler method is used in conjunction with a sufficiently small time-step size varying from 1×10^{-6} to 1×10^{-5} s for particles from 1 to 100 nm.

Results and discussion

Geometry and pressure drop in the nasal-sinus cavity

Thirteen evenly spaced coronal cross-sectional slices were created to allow analysis of geometry and flow characteristics. Figure 2 shows a sample of the cross-sections for the nasal and nasal-sinus computational models. The obvious difference is the larger cross-sectional areas created by the inclusion of the sinuses. There are four pairs of sinuses;

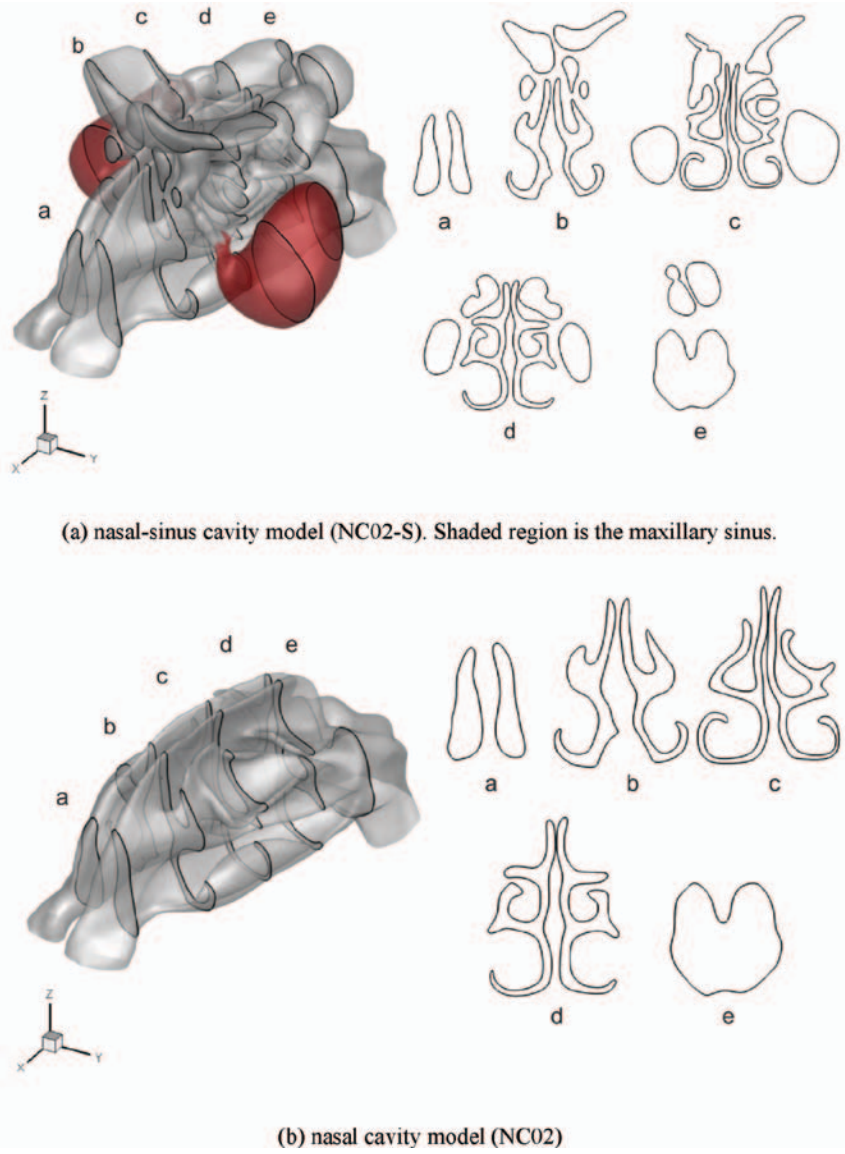

Figure 2. Coronal slices of the airway comparing a (a) nasal cavity with sinus model highlighted by the maxillary sinus and (b) a nasal cavity model with the sinuses omitted.

the maxillary sinuses, located in the cheekbones under the eyes; the frontal sinuses, located in the forehead above the main nasal passages and eyes; the ethmoid sinuses, located between the eyes and the nose and; the sphenoid sinuses, located in the centre of the skull, behind the nose and the eyes. The cross-sectional area versus distance from the anterior tip of the nose to the posterior nasal passage is compared with other nasal cavities published in the literature (Figure 3). The NC02 model (without sinus) has a slightly greater cross-sectional area than other models in the anterior ($x < 4$ cm) and posterior ($x > 6$ cm) region. It is noted that the data from Cheng et al. (1996b) comes from four adult nonsmoking male volunteers (ages 36–57 year), Subramaniam et al. (1998) from a 53-year-old, nonsmoking Caucasian male, and Wen et al. (2008) from a 25 years old, Asian male. The NC02-S model (with sinus) shows a significant increase (up to 300%) in the cross-sectional area, mainly contributed to by the maxillary and frontal sinus. This begins at $x = 0.0187$ cm with the frontal sinuses that protrude superiorly over the nasal passages. Further downstream the presence of maxillary and ethmoid sinuses contributes to the cross-sectional area.

The pressure drop between the nostril inlets and the posterior nasal wall at the nasopharynx for different inhalation rates is shown in Figure 4. Comparisons are made with other published data for nasal cavity (no sinuses) geometries. Currently there are inconsistencies in the representation of the inhalation using CFD in regards to the boundary condition settings for the inlet and outlets. One method is to use pressure inlet and outlet boundary conditions where the nostril inlets are set to gauge pressure, i.e. $P = 0$ Pa and the nasopharynx outlet, a relative negative pressure value corresponding to the inhalation effort created by the diaphragm contraction and expansion of the lungs. This setting is referred to as "pressure" conditions. This differs to a forced flow applied

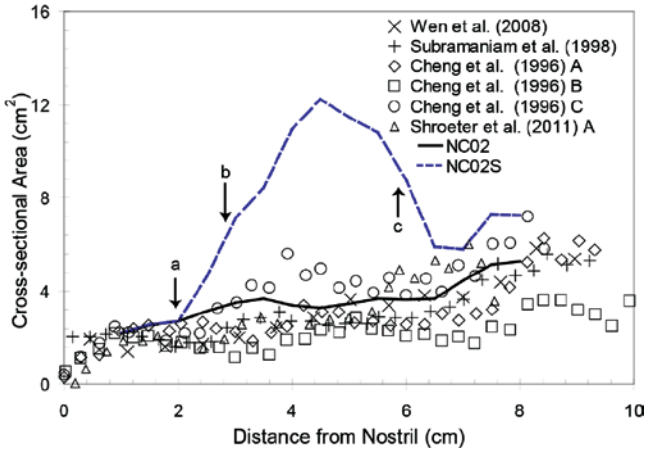

Figure 3. Coronal cross-sectional areas from the nostrils to the posterior nasopharynx in a linear axial vector. The distance from the nostrils at x = 0 cm is taken as the anterior most tip of the nostril opening. Arrow (a) is at x = 0.0187 cm and signifies the beginning of the frontal sinus (b) is at x = 0.0288 cm signifying the anterior beginning of the maxillary sinus, and (c) is at x = 0.0566 cm signifying the posterior end of the maxillary sinus.

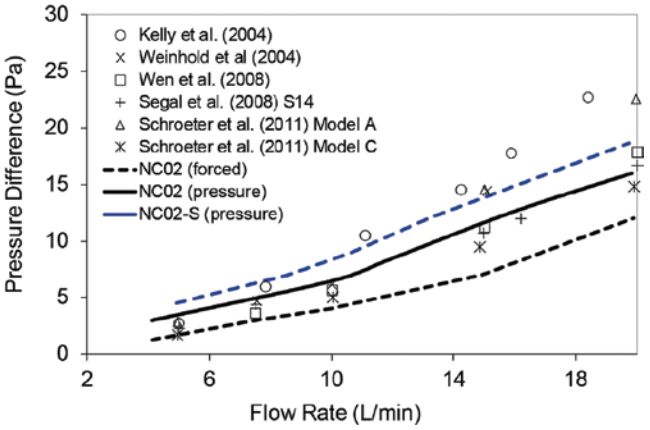

Figure 4. Comparison of the pressure drop for nasal cavity model NCO2 without sinus inclusion.

at the nostril inlets to drive the inhalation. In terms of the numerical boundary conditions this is produced by setting the nostril inlets with equal mass flow distribution (i.e. 5 L/min per nostril for an inhalation rate of 10 L/min) using the mass flow rate or velocity boundary condition, and the nasopharynx outlet as an outflow or opening boundary condition. This setting is labeled as "forced" conditions and its results are compared with the pressure conditions method and also published data in Figure 4. The forced method produces less resistance than the pressure method given that an even distribution of flow passes through both the left and right nasal chambers while the pressure method produces an asymmetric distribution of flow based on the resistance caused by the left and right nasal chamber geometries. A comparison with other nasal cavity geometries shows that the forced method produces less resistance per flow rate. This implies that smaller respiratory effort is required to produce an equivalent inhalation flow rate.

Comparisons of the pressure drop per inhalation flow rate with other models shows that the NC02 model has a flatter profile meaning that it has a lower flow resistance. This is expected given that the cross-sectional area profile of NC02 shown in Figure 3 is larger than the comparative models. The addition of the paranasal sinuses to the nasal cavity produces additional holes or slits in the geometry in the form of the nasal ostium that connects the sinus to the main nasal cavity chambers. Pressure losses in any pipe system are found at openings, especially if part of the opening is aligned with the flow streamlines. As a consequence, additional effort is needed to overcome any pressure that may be lost through the nasal ostia. The pressure difference profile for the NC02-S model shows a steeper curve which implies a larger pressure difference, and hence greater inhalation effort, is required to produce an equivalent inhalation flow rate.

Flow patterns and streamlines

Flow streamlines were released from the left and right nostrils in order to trace the flow patterns. In both instances, the streamlines initially accelerate near the nostril opening before passing mainly through the main nasal passage at mid-height. Some streamlines travel along the floor of the nasal cavity, while some reach the olfactory regions, and up towards the sphenoid and ethomoid sinuses, but these exhibit low velocity ≈ 0.1 m/s as highlighted in Figure 5. These streamlines, based on 100 release points uniformly released across the nostril inlets, do not show any paths leading into the maxilliary sinus, nor the frontal sinus as the release points were uniformly released across the nostril inlets. To determine if any flow will actually pass into the maxillary sinus, we track some path streamlines in reverse from points inside the maxillary sinus.

Figure 6 shows that the flow inside the maxillary sinus occurs at a very low velocity and exhibits typical recirculation of near stagnant flows. Analysis of the geometry and airflow showed that the minimum ostium diameter is 4.6 mm and 3.78 mm, and the pressure difference between the ostium entrance and inside the maxillary sinus are 0.056 Pa and 0.0026 Pa for the left and right sides respectively. The mass flow rate through the left and right ostium is 11.4e-9 kg/s and 6.77e-9 kg/s which are <0.006% of the total inhalation flow rate. This small percentage of flow is not conducive for convective transport of particles into the maxillary sinus and that if any deposition was to occur in this region, then it would be caused by Brownian diffusion. On the other hand the flow streamlines in the sphenoid and ethmoid sinuses are not recirculating but instead convert through with a discernible direction. This suggests that some submicron particles may be transported to this region by convection, enhancing the likelihood of deposition onto the surfaces by diffusion.

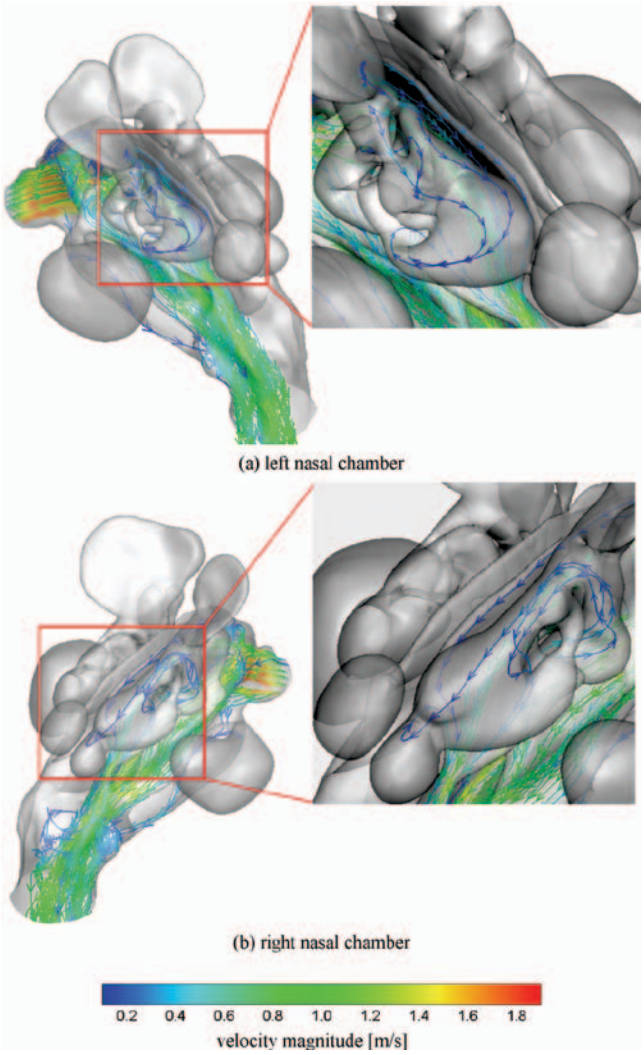

Figure 5. Streamlines passing through the nasal cavity that originates from the (a) left and (b) right nostrils at 10 L/min. Magnified inset highlights the flow streamlines that reach the sphenoid and ethmoid sinus regions.

Contours of velocity magnitude at slices A, B, D, and E (defined in Figure 2) are shown in Figure 7. Slice C is not shown as it produced a similar profile to that of slice D. The 2D contours confirm flow acceleration occurring in the anterior nasal cavity where a peak velocity of 1.8 m/s is found at slice-A. The main flow is centered on the cross-section and pockets of low velocity are found at the top and bottom of the slice. As the flow travels downstream the peak velocity decreases to a value of 1.3 m/s found in slice D. This is due to the airway passage expanding in cross-sectional area resulting in lower velocities. The contours show that the bulk flow regions occur mainly through the mid-height region and close to the nasal septum which separates the two cavities. The contour at slice E shows a well-mixed pattern which is caused by the airflow from the left and right sides of the nasal cavity merging together. Very low flows at <0.1 m/s are found in the sinus regions.

Particle deposition

Preliminary analysis

To test the accuracy of the particle tracking procedure, the flow and particle transport in the entrance region of a pipe and a 90° bend pipe are simulated and the results compared with experimental and analytical solutions. The number of particles tracked through the pipe and nasal cavity geometries was 80,000 (up to 300,000 particles were checked) which was statistically independent from the stochastic nature of the Brownian motion model. The deposition efficiency of ultrafine particles in the range of 1–100 nm was simulated in a straight pipe for a flow rate of 10 L/min, and 5–12 nm particles for a 90° bend pipe. Figure 8 shows the simulated results in comparison with the experimental results from Wang et al. (2002) and the analytical correlation

$$DE = 1 - 0.819\exp(-14.63\Delta) + 0.0976\exp(-89.22\Delta) + 0.0325\exp(-288.0\Delta) + 0.0509\exp\left(-15.9\Delta^{2/3}\right) \quad (10)$$

from Ingham (1975). The Lagrangian particle tracking model that includes the Brownian model with a NWI using Fluent v12.1 is able to handle the diffusion transport in a straight and 90° bend pipe.

The Eulerian model species model which accounts for pure diffusion (i.e. particle inertia effects are excluded), also shows satisfactory results. The Eulerian species simulation is valid for small nanoparticles but with increased flow rate and particle size, the particle inertia becomes important (Xi & Longest, 2008). The deposition efficiency results for a straight pipe with a flow rate of 1 L/min gives a similar trend to that of the 10 L/min flow rate and therefore is not shown for brevity.

Diffusion deposition in the nasal cavity and sinus

Under an inhalation flow rate of 10 L/min, 80000 nanoparticles for each particle size of 1, 5, 10, 40, and 100 nm were tracked within the two nasal cavity models. The total deposition efficiency for the region spanning from the anterior nostril opening conducting airway to the oropharynx is shown in Figure 9. The comparative data comes from different forms of nasal cavity deposition studies which includes *in-vivo* human volunteers by Cheng et al. (1996b), replicate cast models by Kelly et al. (2004), and computational models by Wang et al. (2009) and Zamankhan et al. (2006). The deposition efficiency profile exhibits the ubiquitous decreasing trend as particle size increases for the diffusion deposition of ultrafine particles. For 1 nm particles, there was 99.9% deposition within the nasal cavity. For 10 nm particles the deposition decreases to 24% (NC02) and 30% (NC02-S). At 40 nm the deposition decreases to 6% (NC02) and 9% (NC02-S) and remains at that level as the particle size increases to 100 nm. The decreasing deposition efficiency trend is due to the decreased Brownian excitation of the nanoparticle. A smaller Brownian excitation produces a

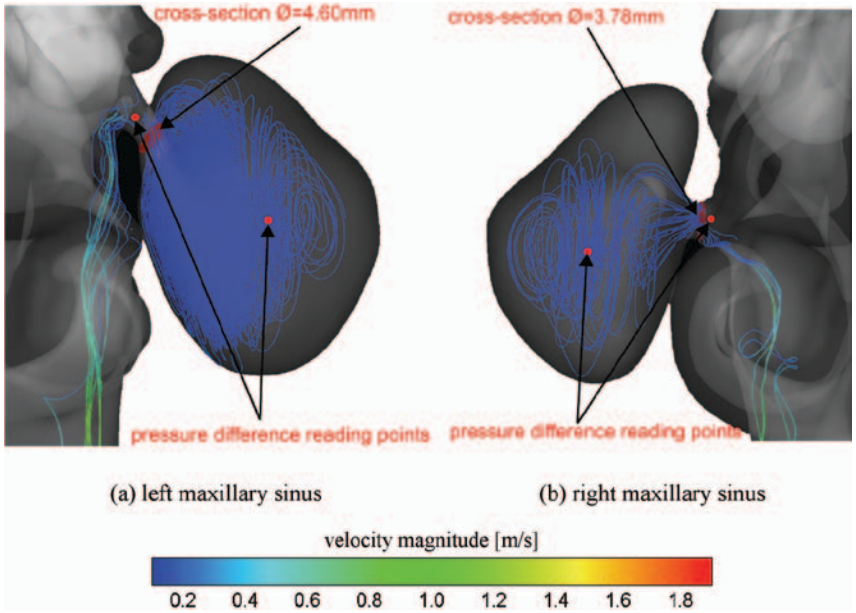

Figure 6. Streamlines passing through the nasal cavity that originates from the (a) left and (b) right nostrils at 10 L/min.

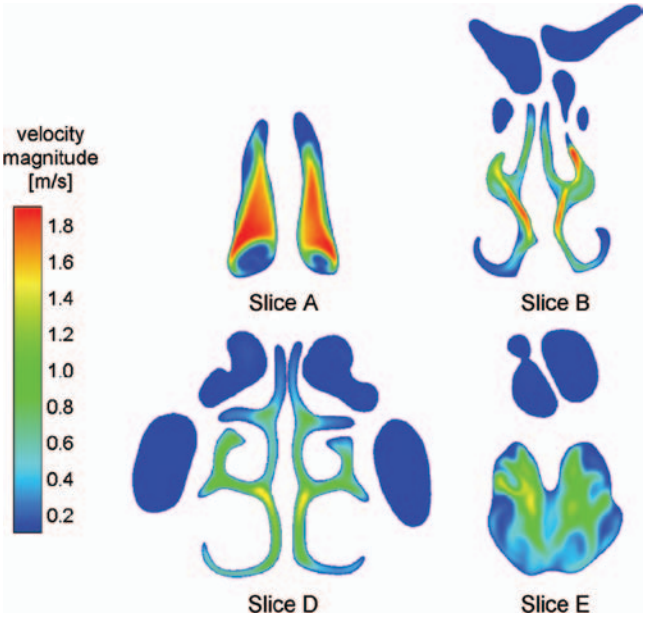

Figure 7. Velocity magnitude contours at 10 L/min.

smaller dispersion, and hence reduces the potential for the particles to diffuse into the ostia and sinus regions. The hypothesis proposed suggests that the deposition efficiency for nasal-sinus cavity model should have a higher value, due to diffusion transport of particles out to the nasal ostia and its sinuses. The results show that there is no difference found for 1 nm particle as both models predict near 100% deposition, while for 10 nm the difference is 6%; 40 nm the difference is 3% and; 100 nm the difference is 2% (Table 2). Therefore, the max deposition difference occurs at 10 nm and this difference reduces as the particles size increase to 100 nm. Larger particles

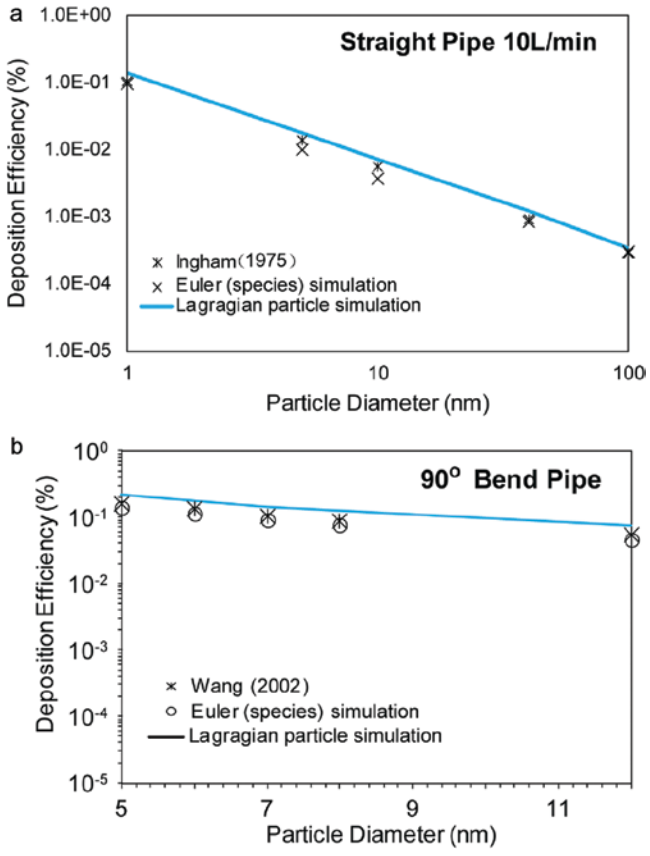

Figure 8. Comparison of deposition efficiency results using the Eulerian species model, Brownian model-Fluent 6.3, and Brownian model-Fluent 12.1 in (a) straight pipe 10 L/min (1 L/min was also performed which produced similar trends) and a (b) 90° bend pipe.

will experience a heightened state of inertia, which convect the particles though the computational domain. The critical value above which inertia significantly influences deposition and transport has been found to be St > 1.0 x 10^{-5} (Xi & Longest, 2008). While the deposition for 1 nm is the same for both models, the deposition may be different. Further analysis, by visualization is provided later to elucidate this.

The maximum difference in deposition efficiency between the two nasal cavity models that occurs is relatively low, when considering the variations between other deposition data, and therefore it may appear that omitting the sinuses for evaluating ultrafine particles may be acceptable. To ensure this we present the deposition efficiency between the two models under a lower flow rate at 4 L/min. From the Pe number which describes the rate of convection to the rate of diffusion by

$$Pe = \frac{U_0 L_h}{\tilde{D}}$$

where U_0 is the characteristic velocity, L_h the characteristic hydraulic length, and $\tilde{D}$ the diffusion coefficient based on the Stokes-Einstein equation, we see that a reduction in flow rate by 2.5× increases the influence of diffusion by the same amount for a given particle size. Figure 10 shows the deposition efficiency for both nasal models where the red color and open symbols represent the sinus NC02-S model. The lines represent the additional 15 L/min case. The black color represents the no sinus NC02 model. The difference in deposition efficiency between the two models at a flow rate of 4 L/min is most significant for 5 nm and 10 nm particles (17% and 16% difference respectively). As the particle size increases the difference between the two models diminishes. For 1 nm particles, the difference is not discernable since the deposition efficiency is nearly at 100%. While the quantifiable difference is not noticeable it is expected that the 1 nm particle diffusion will be much stronger at the lower flow rate of 4 L/min, and that the deposition pattern locally will be different to that at a flow rate of 10 L/min. For completeness the particle deposition efficiency was also evaluated at a flow rate of 15 L/min which shows that the deposition values remain close to a flow rate of 10 L/min for both models. Thus, the differences caused by the sinus geometry remain similar as the flow rate increases from 10 L/min to 15 L/min.

Visualization

To confirm that the 1 nm excitation due to diffusion is much stronger at a lower flow rate, we track each individual particle and record its spatial coordinates after

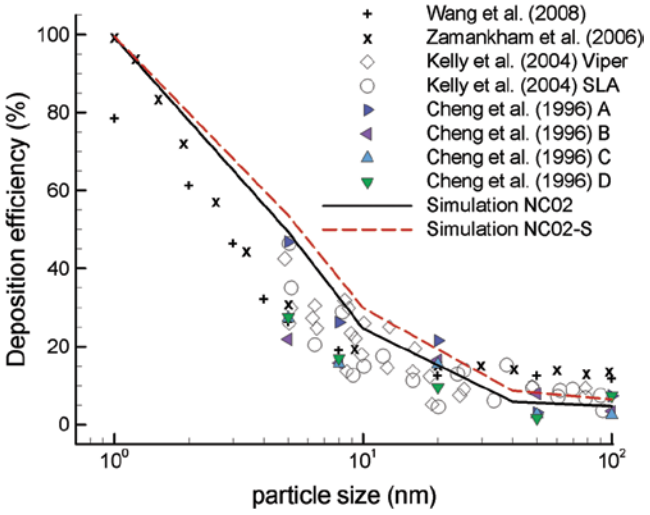

Figure 9. Comparison simulation data for nasal without sinus deposition efficiency for 10 L/min breathing rates.

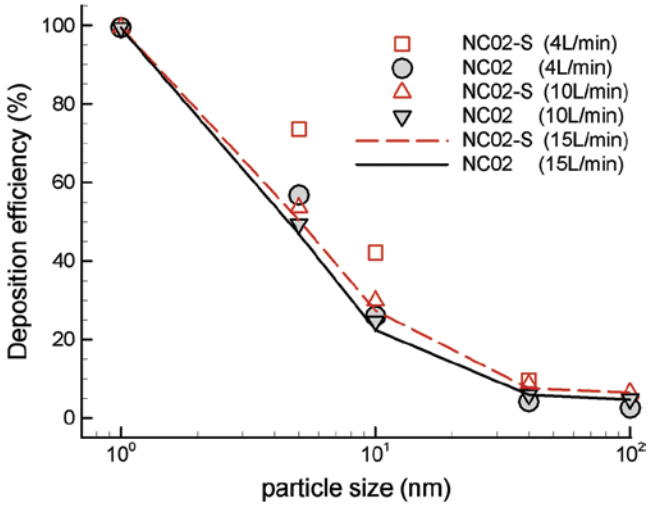

Figure 10. Comparison simulation data for nasal without sinus deposition efficiency for 4 L/min and 10 L/min breathing rates.

Table 2. Summary of geometric characteristics of the nasal cavity.

	Without sinus cavity model				Sinus cavity model	
		Doorly et al. (2008)				
	Present study	Model 1	Model 2	Model 3	Present study	Xiong et al. (2008)
Overall cavity length (cm)	9.7	10.5	10.6	11	9.7	9.1
Overall cavity width (cm)	3.9	–	–	–	7.3	6.6
Surface area (cm^2)	199	106[a]	107[a]	109[a]	290	NA
Volume (cm^3)	NA	13.8	14.2	22.4	NA	NA

[a]Right nasal chamber only.

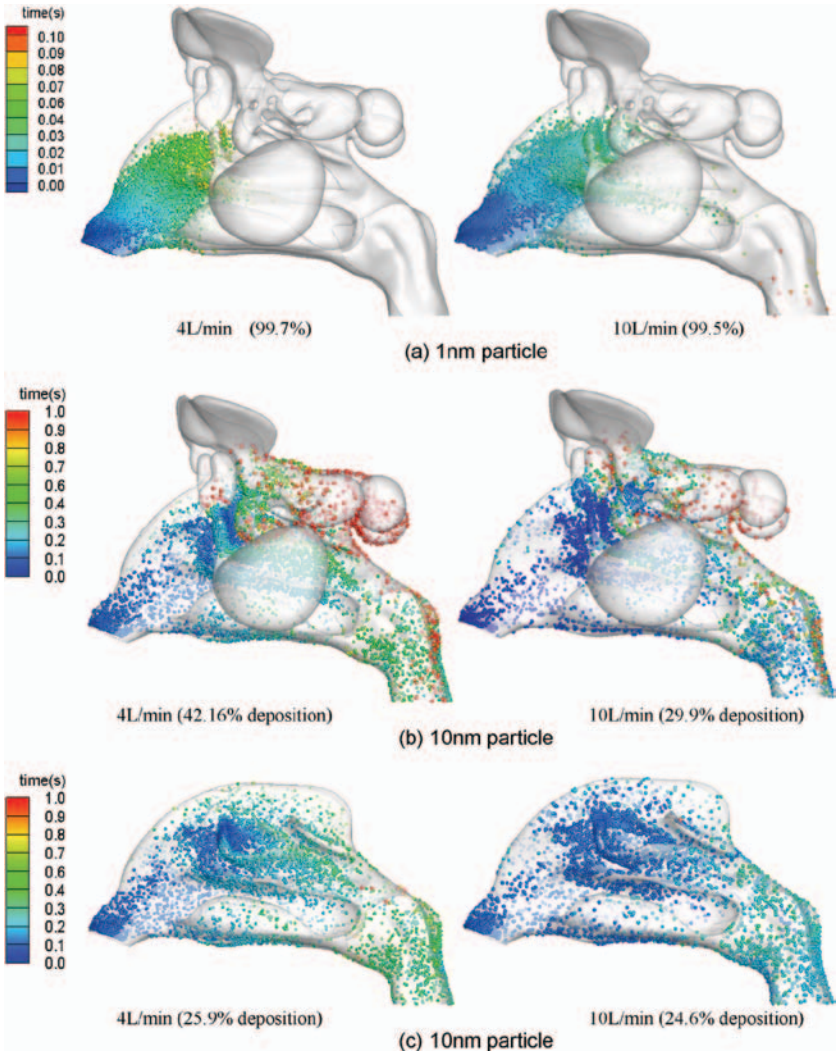

Figure 11. NP deposition pattern in the nasal-sinus cavity for (a) 1 nm, resulting in 98% deposition and (b) 10 nm, resulting in 29.8% deposition. Particles are colored by trajectory time within the nasal cavity before impacting onto the surfaces at 10 L/min.

impaction onto the surrounding surfaces. The coordinates are plotted and colored by residence time as shown in Figure 11. The distribution of 1 nm shows that earlier deposition occurs where a large proportion of the particles persist for less than 0.022 s in the nasal-sinus cavity. The strength or influence of the Brownian diffusion increases as the flow rate decreases, and at a flow rate of 4 L/min, deposition is found within the anterior half of the nasal-sinus cavity while at a flow rate 10 L/min deposition is a little more disperse with deposition sites found in the posterior half.

The deposition pattern for 10 nm particles shows a more random and even distribution pattern. The residence time is 10× as great as that for 1 nm which suggests that the particles are transported with the inhaled flow field for longer and hence has the ability to travel deeper into the nasal cavity and perhaps down towards the lung region. The particle residence time is important for NP deposition studies as it gives an indication of the likelihood of deposition in different regions of the nasal cavity. For example the shorter residence time of 1 nm means that deposition occurs nearly immediately and the deposition zone is restricted to the nasal cavity and further deposition downstream is unlikely. This protects the sensitive lung airways from those NPs that exhibit dangerous properties for respiratory health. Conversely the ability to deposit particles in the middle regions of the nasal cavity or even deeper into the lung airways with high deposition, can be important for therapeutic drug delivery.

Figure 11 is the visual representation of Figure 10. Here we see that the slower flow rate allows increased potential for particle deposition. The comparisons between the two nasal cavity models, NCO2 and NC02-S show that the additional deposition caused by the difference in geometry (i.e. additional paranasal sinuses) occurs in the ethmoid and sphenoid sinus region, and negligible amounts deposit in the maxillary sinus. A possible reason for this particle transport phenomena can be referred back to the convective flow streamlines presented in Figure 5 which showed clear

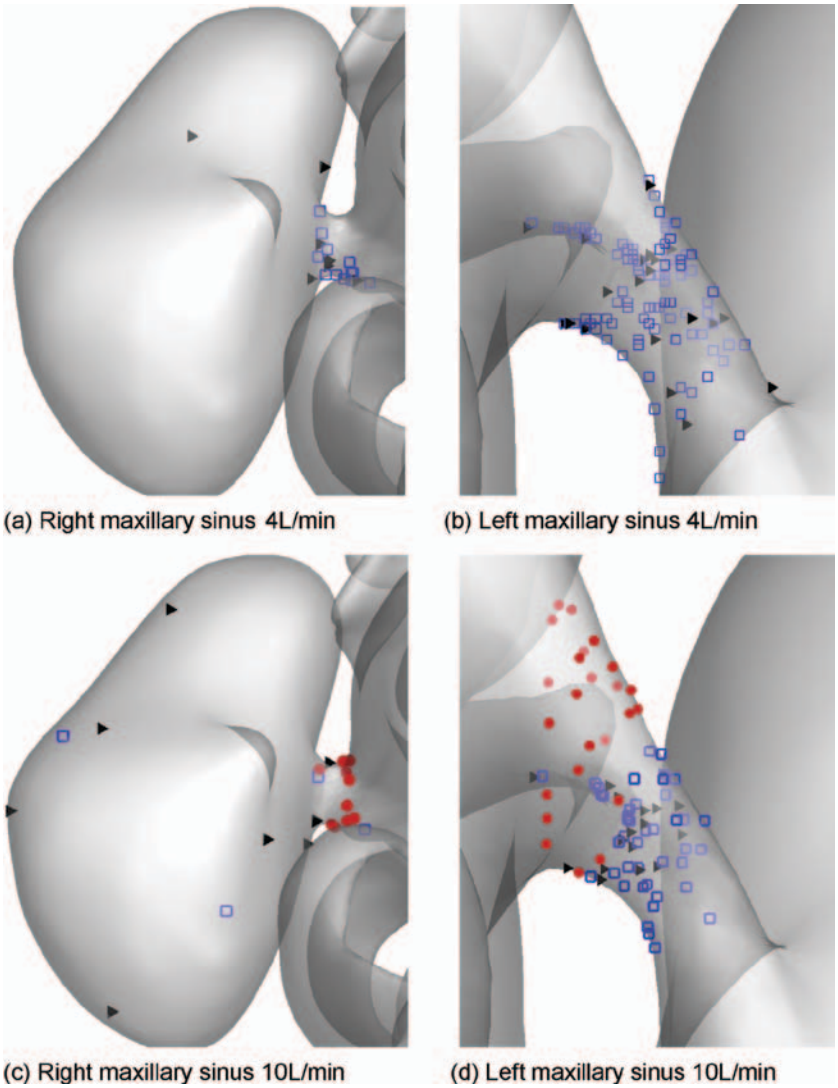

Figure 12. Frontal view showing the NP deposition in maxialliary ostium and sinus for the (a) right nasal cavity, and (b) the left nasal cavity at 10 L/min. Different sized particles are colored as follows: 1 nm red circle; 10 nm blue square; and 40 nm black triangle.

directional streampaths reaching the ethmoid and sphenoid sinuses, albeit at low velocities. This would transport the particles to the superior regions of the nasal cavity and then allow for the diffusion process to occur – a phenomena that allows for the physiological function of olfaction.

Deposition in the maxillary sinus is very low and our hypothesis that the diffusion process may be dominant enough for particles to pass into the paranasal sinuses appears to only be supported if there is some convection involved (e.g. deposition sites in the sphenoid and ethmoid sinuses). In the maxillary sinuses the ostium protrudes at nearly right angles to the main flow field. To further investigate this we examine the maxillary ostium and locate the deposition of individual 1 nm, 10 nm and 40 nm particles within the region as shown in Figure 12. In the right maxilliary sinus, inclusive of the ostium, a small percentage of particles <0.04% are deposited. At a flow rate of 4 L/min there are no 1 nm particles depositing due to its early deposition in the main nasal passage. For both models, 10 nm and 40 nm particles are found concentrated within the ostium. Thus it appears that despite a lower flow rate, there is a lack of particle deposition within the maxillary sinus.

For a flow rate of 10 L/min it can be seen that 1 nm particles are captured within the narrow ostium and in fact don't make it through to the maxilliary sinus. For the left maxilliary sinus, no particles were able to pass through the ostium, but a larger percentage of particles <0.5% deposited within the ostium alone. This is mainly due to the curved geometry and longer ostium length providing a narrow tube passageway for the particles to diffuse onto. These results support the report by Hood et al. (2009), that ostium sinus ventilation is limited (unless the ostium is very large) and that the gas exchange of nitric oxide (NO) between the air in the maxillary sinus and the nasal air does not contributor greatly to the overall NO concentration.

In this study, the passageway into the paranasal sinuses via the ostia were open, and obstruction was not included in the model. At this stage no data exists for the type and amount of blockage that is typical of sinusitis. However in such a case, any inflammation and hence obstruction within the main nasal passage will cause sharper accelerations and more erratic flow behavior to the air and particle flows, while obstructions in the ostia and paranasal sinuses may not influence the bulk flow but will influence the nitric oxide gas exchange within the sinuses (Hood et al., 2009).

Study limitations and future study

This study used only a single subject's nasal airway and paranasal sinuses which has limitations due to the inter-subject variability in anatomy between different people. Further studies may examine the differences in a wide range of subjects and with a larger sample size (age, sex, ethnicity etc.). However in general, gross flow features and overall particle deposition can provide sufficient insight into the trends that are consistent among different geometries. On the assumption that the subject within this study is without pathology and representative of an "average" patient, the preliminary results from this study will aid in gaining an appropriate understanding of the effect of paranasal sinuses on nanoparticle deposition.

This current study focuses on the deposition of NPs in healthy subjects and the potential of these particles to cause pathology like sinusitis. Chronic sinusitis is a common problem in our population with a prevalence in the United States of 14.6% and results in significant morbidity, costing the US health care system approx. $3.4–5 billion annually (Pleis et al., 2009). There is potential in future work to speculate the implications of sinusitis and obstruction of paranasal sinuses on particle flow and deposition in the nasal airways. These results may be applicable to improving novel delivery of therapies to treat conditions like chronic sinusitis.

Conclusion

A nasal cavity model including the sinuses was created in order to determine if any NPs would deposit within the paranasal sinuses given that these particles are transported through the nasal cavity mainly by diffusion. Under a flow rate of 10 L/min it was shown that 1 nm particles deposited early and in the anterior half of nasal cavity with a deposition efficiency of 99%. As the particle increased in size to 10 nm the diffusive nature of the NP decreased and the deposition efficiency reduced to 30%. However a more evenly distributed deposition pattern was found for 10 nm particles. The effect of including the sinus compartments with the nasal geometry on the deposition efficiency was most significant for 10 nm particles. This difference is further amplified when the flow rate is decreased which allows the diffusion to be more influential. These results aimed to identify the possible differences that may occur when evaluating particle inhalation for toxicology or drug delivery using cast or computational models that exclude the sinus regions. This is particularly important for the case where flow rates are low and particle sizes are around 5–10 nm particle sizes and comparative studies between human subjects and nasal cavity cast or CFD models that neglect the sinus airways should consider the diffusion effects of nanoparticles. It was noted that this study only looked at one subject, so future work in this field will be required to look at the variable anatomy between different patients and its effect on simulation results. In addition, there is room for future research using models of patients with pathology, such as sinusitis, where there is partial loss of paranasal sinuses and ostia obstruction. Results from this work will have high clinical relevance for sufferers of these chronic conditions.

Declaration of interest

The authors would like to gratefully acknowledge the financial support provided by the National Basic Research Program (973) of China, Grant No. 2012CB720100 and the Australian Research Council (project ID: DP120103958).

References

Auffan M, Rose J, Bottero JY, Lowry GV, Jolivet JP, Wiesner MR. 2009. Towards a definition of inorganic nanoparticles from an environmental, health and safety perspective. Nat Nanotechnol 4:634–641.

Calderón-Garcidueñas L, Delgado R, Calderón-Garcidueñas A, Meneses A, Ruiz LM, De La Garza J, Acuna H, Villarreal-Calderón A, Raab-Traub N, Devlin R. 2000. Malignant neoplasms of the nasal cavity and paranasal sinuses: A series of 256 patients in Mexico City and Monterrey. Is air pollution the missing link? Otolaryngol Head Neck Surg 122:499–508.

Cheng K-H, Cheng Y-S, Yeh H-C, Swift DL. 1995. Deposition of ultrafine aerosols in the head airways during natural breathing and during simulated breath holding using replicate human upper airway casts. Aerosol Sci Tech 23:465–474.

Cheng KH, Cheng YS, Yeh HC, Guilmette A, Simpson SQ, Yang YH, Swift DL. 1996a. *In-vivo* measurements of nasal airway dimensions and ultrafine aerosol deposition in the human nasal and oral airways. J Aerosol Sci 27:785–801.

Cheng YS, Yeh HC, Guilmette RA, Simpson SQ, Cheng KH, Swift DL. 1996b. Nasal deposition of ultrafine particles in human volunteers and its relationship to airway geometry. Aerosol Sci Tech 25:274–291.

Cheng YS, Holmes TD, Gao J, Guilmette RA, Li S, Surakitbanharn Y, Rowlings C. 2001. Characterization of nasal spray pumps and deposition pattern in a replica of the human nasal airway. J Aerosol Med 14:267–280.

Churchill SE, Shackelford LL, Georgi JN, Black MT. 2004. Morphological variation and airflow dynamics in the human nose. Am J Hum Biol 16:625–638.

Doorly DJ, Taylor DJ, Gambaruto AM, Schroter RC, Tolley N. 2008. Nasal architecture: form and flow. Phil Trans Math Phys Eng Sci 366:3225–3246.

Elwood JM. 1981. Wood exposure and smoking: Association with cancer of the nasal cavity and paranasal sinuses in British Columbia. Can Med Assoc J 124:1573–1577.

Garcia GJ, Bailie N, Martins DA, Kimbell JS. 2007. Atrophic rhinitis: A CFD study of air conditioning in the nasal cavity. J Appl Physiol 103:1082–1092.

Hahn I, Scherer PW, Mozell MM. 1993. Velocity profiles measured for airflow through a large-scale model of the human nasal cavity. J Appl Physiol 75:2273–2287.

Halperin WE, Goodman M, Stayner L, Elliott LJ, Keenlyside RA, Landrigan PJ. 1983. Nasal cancer in a worker exposed to formaldehyde. JAMA 249:510–512.

Hood CM, Schroter RC, Doorly DJ, Blenke EJ, Tolley NS. 2009. Computational modeling of flow and gas exchange in models of the human maxillary sinus. J Appl Physiol 107:1195–1203.

Ingham DB. 1975. Diffusion of aerosols from a stream flowing through a cylindrical tube. J Aerosol Sci 6:125–132.

Inthavong K, Tian ZF, Li HF, Tu JY, Yang W, Xue CL, Li CG. 2006. A numerical study of spray particle deposition in a human nasal cavity. Aerosol Sci Techn 40:1034–1045.

Inthavong K, Ge Q, Se CMK, Yang W, Tu JY. 2011a. Simulation of sprayed particle deposition in a human nasal cavity including a nasal spray device. J Aerosol Sci 42:100–113.

Inthavong K, Zhang K, Tu J. 2011b. Numerical modelling of nanoparticle deposition in the nasal cavity and the tracheobronchial airway. Comput Methods Biomech Biomed Engin 14:633–643.

Keir J. 2009. Why do we have paranasal sinuses? J Laryngol Otol 123:4–8.

Kelly JT, Prasad AK, Wexler AS. 2000. Detailed flow patterns in the nasal cavity. J Appl Physiol 89:323–337.

Kelly J, Asgharian B, Kimbell J, Wong B. 2004. Particle deposition in human nasal airway replicas manufactured by different methods. Part II: Ultrafine particles. Aerosol Sci Tech 38:1072–1079.

Lindemann J, Brambs HJ, Keck T, Wiesmiller KM, Rettinger G, Pless D. 2005. Numerical simulation of intranasal airflow after radical sinus surgery. Am J Otolaryngol 26:175–180.

Longest PW, Xi J. 2007a. Computational investigation of particle inertia effects on submicron aerosol deposition in the respiratory tract. J Aerosol Sci 38:111–130.

Longest PW, Xi J. 2007b. Effectiveness of direct Lagrangian tracking models for simulating nanoparticle deposition in the upper airways. Aerosol Sci Tech 41:380–397.

Ounis H, Ahmadi G, McLaughlin JB. 1991. Brownian diffusion of submicrometer particles in the viscous sublayer. J Colloid Interface Sci 143:266–277.

Pleis JR, Lucas JW, Ward BW. 2009. Summary health statistics for U.S. adults: National Health Interview Survey, 2008. Vital Health Stat 10:1–157.

Robert GH. 2001. Forced inspiratory nasal flow–volume curves: A simple test of nasal airflow. Mayo Clin Proc 76:990–994.

Schroeter JD, Kimbell JS, Asgharian B. 2006a. Analysis of particle deposition in the turbinate and olfactory regions using a human nasal computational fluid dynamics model. J Aerosol Med 19:301–313.

Schroeter JD, Kimbell JS, Asgharian B. 2006b. Analysis of particle deposition in the turbinate and olfactory regions using a human nasal computational fluid dynamics model. J Aerosol Med 19:301–313.

Schroeter JD, Garcia GJ, Kimbell JS. 2011. Effects of Surface Smoothness on Inertial Particle Deposition in Human Nasal Models. J Aerosol Sci 42:52–63.

Shi H, Kleinstreuer C, Zhang Z. 2008. Dilute suspension flow with nanoparticle deposition in a representative nasal airway model. Phys Fluid 20:1–23.

Slavin RG. 1988. Sinusitis in adults and its relation to allergic rhinitis, asthma, and nasal polyps. J Allergy Clin Immunol82:950–956.

Subramaniam RP, Richardson RB, Morgan KT, Kimbell JS, Guilmette RA. 1998. Computational fluid dynamics simulations of inspiratory airflow in the human nose and nasopharynx. Inhal Toxicol 10:91–120.

Swift DL, Proctor DF. 1977. Access of air to the respiratory tract. In: Brain JD, Proctor DF, Reid LM, eds. Respiratory Defense Mechanism. New York: Marcel Dekker, 63–93.

Wang J, Flagan RC, Seinfeld JH. 2002. Diffusional losses in particle sampling systems containing bends and elbows. J Aerosol Sci 33:843–857.

Wang SM, Inthavong K, Wen J, Tu JY, Xue CL. 2009. Comparison of micron- and nanoparticle deposition patterns in a realistic human nasal cavity. Respir Physiol Neurobiol 166:142–151.

Wen J, Inthavong K, Tu J, Wang S. 2008. Numerical simulations for detailed airflow dynamics in a human nasal cavity. Respir Physiol Neurobiol 161:125–135.

Xi J, Longest PW. 2008. Numerical predictions of submicrometer aerosol deposition in the nasal cavity using a novel drift flux approach. Int J Heat and Mass Tran 51:5562–5577.

Xiong GX, Zhan JM, Jiang HY, Li JF, Rong LW, Xu G, Xu G. 2008. Computational fluid dynamics simulation of airflow in the normal nasal cavity and paranasal sinuses. Am J Rhinol 22:477–482.

Zamankhan P, Ahmadi G, Wang Z, Hopke PH, Cheng YS, Su WC, Leonard D. 2006. Airflow and deposition of nanoparticles in a human nasal cavity. Aerosol Science Technol 40:463–476.